

**A Generalization of the Two Dimensional Prolate Spheroidal Wave Function Method for  
Non-rectilinear MRI data Acquisition Methods**

**Martin A. Lindquist<sup>1</sup>, Cun-Hui Zhang<sup>2</sup>, Gary Glover<sup>3</sup>, Lawrence Shepp<sup>2</sup>, Qing. X. Yang<sup>4</sup>**

<sup>1</sup> Department of Statistics, Columbia University, New York, NY, 10027 (martin@stat.columbia.edu)

<sup>2</sup> Department of Statistics, Rutgers University, New Brunswick, NJ, 08854

<sup>3</sup> Department of Radiology, Lucas MR Center, Stanford University, Stanford, CA, 94305

<sup>4</sup> Department of Radiology (Center for NMR Research), The Pennsylvania State University, College of Medicine, The Milton S. Hershey Medical Center, Hershey, PA, 17033.

**EDICS:** 3MRIM – Magnetic Resonance Imaging

**RUNNING TITLE:** Generalized 2D-PSWF Method

## **ABSTRACT**

The two-dimensional Prolate Spheroidal Wave Function (2D-PSWF) method was previously introduced as an efficient method for trading-off between spatial and temporal resolution in magnetic resonance imaging (MRI), with minimal penalty due to truncation and partial volume effects. In the 2D-PSWF method, the k-space sampling area and a matching 2D-PSWF filter, with optimal signal concentration and minimal truncation artifacts, are determined by the shape and size of a given convex region of interest (ROI). The spatial information in the reduced k-space data is used to calculate the total image intensity over a non-square ROI instead of producing a low-resolution image. This method can be used for tracking dynamic signals from non-square ROIs using a reduced k-space sampling area, while achieving minimal signal leakage. However, the previous theory is limited to the case of rectilinear sampling. In order to make the 2D-PSWF method more suitable for dynamic studies, this paper presents a generalized version of the 2D-PSWF theory that can be applied to non-rectilinear data acquisition methods. The method is applied to an fMRI study using a spiral trajectory, which illustrates the method's efficiency at tracking hemodynamic signals with high temporal resolution.

**Key Words:** magnetic resonance imaging, signal processing, non-uniform k-space sampling, prolate spheroidal wave function, rapid data acquisition.

## INTRODUCTION

Magnetic resonance imaging (MRI) signals (raw data) are acquired in the frequency-domain (k-space), which is typically sampled on a rectangular Cartesian grid, and then Fourier transformed into the spatial-domain (image-space). A trade-off between spatial and temporal resolution is often used to increase the image sampling speed required by many dynamic applications [1]-[6]. However, reduction of spatial resolution in an image leads to a stronger partial-volume effect, which decreases the sensitivity of dynamic signals. These problems are frequently encountered in rapid imaging and chemical shift imaging. The origin of the problem is the disparity between the size and irregular geometry of the region of interest (ROI), and the rectangular voxel produced by the fast Fourier transform [7].

In order to solve this problem, the two dimensional Prolate Spheroidal Wave Function (2D-PSWF) method was developed to address the issues inherent in the fast Fourier transform [8]-[12]. To efficiently reduce the number of acquired data points, the 2D-PSWF method tailors the k-space sampling area according to the size and shape of a predetermined convex ROI and creates a matching 2D-PSWF filter to optimally reduce truncation effects. In this method, the spatial information in the reduced k-space data is used to calculate the total signal intensity over a non-square ROI instead of producing a low-resolution image. This method is ideally suited for localized spectroscopy and tracking dynamic signals from non-square ROIs using a reduced k-space sampling area, while achieving minimal signal leakage.

Because hardware restrictions (gradient strength and slew rate) and the threshold of neuro-stimulation by rapidly switching gradients set a physical limit for image acquisition rates, non-rectilinear data acquisition methods such as radial and spiral imaging are often employed. For these sampling schemes k-space is sampled non-uniformly and the sampling points do not lie on a rectangular grid. The original 2D-PSWF theory was developed only for the rectilinear sampling case. To further develop the 2D-PSWF method to increase its suitability for dynamic MRI and CSI studies, this paper presents a generalized 2D-PSWF theory that can be applied to non-rectilinear data acquisition methods. An example of its implementation for dynamic MRI is presented using a spiral k-space sampling method.

## THEORY

### I. Fast fMRI using the 2D-PSWF

Let us begin with a brief review of the basic theory of the 2D-PSWF in the context of its application to fMRI before proceeding to develop the general case. As k-space consists of a sequence of discrete measurements during MRI data acquisition, it should therefore be chosen to be discrete. On the other hand, image-space, denoted by  $\Omega$  in this paper, can be chosen to be either discrete or continuous. In previous applications of the 2D-PSWF theory to fMRI [8]–[12], image-space was defined as a discrete space consisting of a collection of image elements (voxels). For an  $N \times N$  image, the space consists of  $N^2$  elements. However, it may be more advantageous to instead treat image-space as continuous, as the underlying object being imaged should be considered continuous. Fig.1 gives an illustration of both approaches towards setting up the problem formulation. In this section we focus on the discrete/continuous case, as the discrete/discrete case has already been studied extensively in previous work [8]–[12].

Consider a convex ROI,  $B$ , in image-space. The objective of the 2D-PSWF method is to determine the optimal sampling region in k-space,  $A$ , of a predetermined size  $a$ , which maximizes the total signal over the region  $B$  in image-space (Fig. 1b). This is achieved by designing a k-space sampling region based on the size and shape of given  $B$ , and combining this with a matched two-dimensional filter that maximizes the energy concentration in  $B$ . The key to the method is finding the matched filter function  $g(\mathbf{k})$ , that satisfies the following two criteria:

- (i) It takes the value 0 for points outside of  $A$ .
- (ii) Its inverse Fourier transform,  $G(\mathbf{x})$ , has maximal signal concentration in  $B$ , i.e. the ratio

$$\lambda = \frac{\int_B |G(\mathbf{x})|^2 d\mathbf{x}}{\int_{\Omega} |G(\mathbf{x})|^2 d\mathbf{x}} \quad (1)$$

is maximized over all possible functions for which criterion (i) holds.

As an additional constraint, the denominator of the ratio in (1) is set equal to one. This simplifies the problem to finding the function,  $g(\mathbf{k})$ , with norm equal to one, whose inverse Fourier transform maximizes,

$$\lambda = \int_B |G(\mathbf{x})|^2 d\mathbf{x} . \quad (2)$$

The problem of finding  $g(\mathbf{k})$  is a 2D generalization of the theory of Prolate Spheroidal Wave Functions (PSWF) [13]-[18]. Using Parseval's identity, the problem can be written in matrix form as,

$$\lambda = \max \{ \mathbf{g}^+ \mathbf{K}_{A,B} \mathbf{g} \} \quad (3)$$

under the constraint,

$$\mathbf{g}^+ \mathbf{g} = \sum_{\mathbf{k}_j \in A} g(\mathbf{k}_j) \overline{g(\mathbf{k}_j)} = 1 . \quad (4)$$

Suppose  $\mathbf{K}_B$  is the Fourier transform of the indicator function of the region  $B$ , denoted  $I_B$ , which can be written:

$$\begin{aligned} K_B(\mathbf{k}) &= \int_B \exp\{-2\pi i(\mathbf{x}, \mathbf{k})\} d\mathbf{x} \\ &= \hat{I}_B(\mathbf{k}) . \end{aligned} \quad (5)$$

Then it can be shown that the kernel,  $\mathbf{K}_{A,B}$ , is given by,

$$\mathbf{K}_{A,B}(\mathbf{k}, \mathbf{k}') = \mathbf{K}_B(\mathbf{k} - \mathbf{k}') \quad (6)$$

for  $\mathbf{k}, \mathbf{k}' \in A$ . For simple regions  $B$  (e.g. circles, squares, ellipses) there exist analytical expressions for  $\hat{I}_B$ , which allow for easy computation of the kernel defined in (6). The solution to the problem stated in (3) is the largest eigenvector of the matrix  $\mathbf{K}_{A,B}$ . The corresponding largest eigenvalue,  $\lambda$ , provides a quantitative measure of the signal leakage that the eigenvector gives rise to. A value of  $\lambda$  close to 1 indicates little signal leakage, while the leakage increases as  $\lambda$  decreases.

It can be shown in an analogous manner that for the case when image-space is instead considered discrete (Fig. 1a), the problem becomes finding the largest eigenfunction of the  $a \times a$  matrix with elements given by,

$$K_{A,B}(\mathbf{k}, \mathbf{k}') = \frac{1}{N^2} \sum_{\mathbf{x} \in B} \exp\left\{-\frac{2\pi i}{N}(\mathbf{x}, \mathbf{k} - \mathbf{k}')\right\} \quad (7)$$

for  $\mathbf{k}, \mathbf{k}' \in A$ .

Once we calculate the optimal filter corresponding to some fixed  $A$ , for a given  $B$ , we let  $A$  vary among all possible k-space regions of a given size  $a$ . For each possible region we obtain a corresponding vector  $g(\mathbf{k}, A)$  for which the stated criteria hold. Finally we choose the region whose corresponding  $g(\mathbf{k}, A)$  makes the maximal concentration ratio,  $\lambda$ , as large as possible. The problem of finding the optimal sampling region  $A$  is a difficult mathematical problem, as it involves an exponential growth in  $N$  computer searches for an  $N \times N$  size image. To avoid such an extremely computer-intensive search, a heuristic sampling scheme is introduced in [10], which computer searches show to be near-optimal. In addition it can be shown that the optimal choice of  $A$ , when  $B$  is a circle, is a circular region in k-space.

This choice coincides with the heuristic scheme, which for the convex regions  $B$  typically used in this method winds up giving re-scaled and rotated versions of  $B$  centered in the middle of  $k$ -space.

It should be noted that in one dimension, one has an associated differential operator with the same eigenfunctions [13-16], which can be used to deduce conditions for when the multiplicity of the largest eigenvalue is equal to one. However, in higher dimensions such conditions do not exist and if we are not careful we may not have a unique eigenfunction, and hence have more than one answer to the maximization problem stated in (3). If the multiplicity of the largest eigenvalue is greater than one, it is beneficial to shrink the size of the sampling region  $A$  until the relationship  $\lambda_2 \ll \lambda_1 \approx 1$  holds. Experiment shows that we are able to consistently obtain a dominant eigenvalue that has multiplicity one, for appropriate regions, using this approach. Fig. 2 shows a plot of the two largest eigenvalues for the case when  $B$  is a small circular region with fixed radius (radius = 7.5mm, FOV = 200mm) and  $A$  is a circular region with variable radius, containing  $a$  equally spaced  $k$ -space measurements. As  $a$  increases it is clear from Fig. 2 that the value of the two largest eigenvalues both approach 1. However, as the largest eigenvalue increases faster, there exists a range of values for  $a$ , such that the largest eigenvalue is equal to one and the second largest is significantly below 1. In this particular example this corresponds to a region consisting of approximately 800 points in  $k$ -space. This value indicates an appropriate size,  $a$ , for the sampling region  $A$ .

Once we have calculated the 2D-PSWF filter  $g(\mathbf{k})$ , the next step is to apply it to the raw data. Let us assume that  $f(\mathbf{k})$  is an experimental sampling function in  $k$ -space and  $F(\mathbf{x})$  is its corresponding Fourier transform (the image). It can be shown [8]-[9] that we can calculate the integral of the signal intensity over  $B$ ,  $F_B$ , using the formula:

$$F_B = \int_B F(\mathbf{x}) d\mathbf{x} \propto \sum_{\mathbf{k}_j \in A} f(\mathbf{k}_j) \overline{g(\mathbf{k}_j)} \quad (8)$$

as long as  $g(\mathbf{k}) > 0$  on  $A$ , which holds for the convex regions that we have studied. Equation (8) shows that the integral of the image intensity over  $B$  can be approximated using a reduced area of k-space,  $\mathbf{k} \in A$ , since  $g(\mathbf{k}) = 0$  outside of  $A$ . Thus, if we are interested in obtaining the total signal intensity over a given ROI in an image, the sampling of k-space can be reduced to a region  $A$ .

A 2D-PSWF filter calculated for a specific  $B$  at  $\mathbf{x}$  can be used for all translationally shifted ROIs in image space. An alternative ROI at  $\mathbf{x} + \mathbf{s}$  can be obtained by shifting  $B(\mathbf{x})$  to  $B(\mathbf{x} + \mathbf{s})$  in image-space, where  $\mathbf{s}$  is a displacement vector. The signal intensity over the new ROI can be calculated as follows:

$$F_B(\mathbf{s}) \propto \sum_{\mathbf{k}_j \in A} f(\mathbf{k}_j) \overline{g(\mathbf{k}_j)} e^{i2\pi(\mathbf{s}, \mathbf{k}_j)}. \quad (9)$$

Thus,  $A$  and the associated function  $g(\mathbf{k})$  can be used for calculation of any ROI with the same shape and size. Therefore having prior knowledge of the exact location of an ROI is of less importance, as one can simply shift the ROI if necessary during post-processing.

## II. The non-uniform sampling case.

As the 2D-PSWF method often requires one to sample non-square regions in k-space, it is often more efficient to use a trajectory that samples k-space non-uniformly. However, it can be shown that the PSWF operator shown in (6) no longer yields the correct solution for the case when the k-space region  $A$  is sampled non-uniformly. Note that throughout we assume that image-space is continuous and without loss of generality that  $\Omega$  is a unit square.

When calculating the PSWF function, the denominator of the ratio in (1) is set equal to one. In the case when the data is sampled on a Cartesian grid, this implies that

$$\sum_{\mathbf{k}_j \in A} |g(\mathbf{k}_j)|^2 = 1 \quad , \quad (10)$$

which is an essential constraint for the derivation of (6) to hold. In the case when k-space is sampled non-uniformly (10) no longer holds. To see why, let us take a closer look at the denominator of the ratio in (1),

$$\begin{aligned} \int_{\Omega} |G(\mathbf{x})|^2 d\mathbf{x} &= \int_{\Omega} G(\mathbf{x}) \overline{G(\mathbf{x})} d\mathbf{x} \\ &= \int_{\Omega} \left( \sum_{\mathbf{k} \in A} g(\mathbf{k}) e^{i2\pi(\mathbf{x}, \mathbf{k})} \right) \overline{\left( \sum_{\mathbf{l} \in A} g(\mathbf{l}) e^{i2\pi(\mathbf{x}, \mathbf{l})} \right)} d\mathbf{x} \\ &= \sum_{\mathbf{k} \in A} \sum_{\mathbf{l} \in A} g(\mathbf{k}) \overline{g(\mathbf{l})} \left( \int_{\Omega} e^{i2\pi(\mathbf{x}, \mathbf{k} - \mathbf{l})} d\mathbf{x} \right) \\ &= \sum_{\mathbf{k} \in A} \sum_{\mathbf{l} \in A} g(\mathbf{k}) \overline{g(\mathbf{l})} K(\mathbf{k}, \mathbf{l}) \end{aligned} \quad (11)$$

where

$$K(\mathbf{k}, \mathbf{l}) = \int_{\Omega} e^{i2\pi(\mathbf{x}, \mathbf{k} - \mathbf{l})} d\mathbf{x} . \quad (12)$$

When the k-space points  $\mathbf{k}$  and  $\mathbf{l}$  lay on the Cartesian grid, we have that

$$K(\mathbf{k}, \mathbf{l}) = \begin{cases} 1 & \text{if } \mathbf{k} = \mathbf{l} \\ 0 & \text{if } \mathbf{k} \neq \mathbf{l} \end{cases} \quad (13)$$

Hence,

$$\sum_{\mathbf{k} \in A} \sum_{\mathbf{l} \in A} g(\mathbf{k}) \overline{g(\mathbf{l})} K(\mathbf{k}, \mathbf{l}) = \sum_{\mathbf{k} \in A} |g(\mathbf{k})|^2 \quad (14)$$

and thus

$$\sum_{\mathbf{k} \in A} |g(\mathbf{k})|^2 = 1, \quad (15)$$

which implies that (10) will hold. However, when the coordinates  $\mathbf{k}$  and  $\mathbf{l}$  do not lie on the Cartesian grid, this relationship will not hold. Hence, when dealing with the non-uniform case we will have to take the kernel,  $\mathbf{K}$ , into consideration while deriving the PSWF filter.

### III. The generalized prolate spheroidal wave function for non-uniform sampling

Assume that we non-uniformly sample a finite set of points in k-space  $\mathbf{k}_1, \mathbf{k}_2, \dots, \mathbf{k}_a$ , which we will refer to as  $A$ . In MRI, the measured signal at point  $\mathbf{k}_j$ ,  $S(\mathbf{k}_j)$ , is related to the image function  $F(\mathbf{x})$  according to the relationship:

$$S(\mathbf{k}_j) = C \int_{\Omega} F(\mathbf{x}) e^{-i2\pi(\mathbf{x}, \mathbf{k}_j)} d\mathbf{x} \quad \text{for } j=1, \dots, N, \quad (16)$$

where  $C$  is a constant and  $\Omega$  denotes image space. This equation shows that  $S(\mathbf{k}_j)$  is a multiple of the Fourier transform of the image function. For notational simplicity we will assume the constant is equal to 1 and will subsequently refer to  $S(\mathbf{k}_j)$  as  $f(\mathbf{k}_j)$ .

Now, consider a function  $p(\mathbf{k})$  which is zero outside of  $A$  and whose inverse Fourier transform has its energy maximally concentrated on a region  $B$  in image-space. That is,  $p(\mathbf{k})$  is zero for any point lying outside of  $A$ , and its inverse Fourier transform maximizes the ratio given in (1). Suppose we apply this function to the sampled data in the same manner described in the previous section. Following (9), we can calculate the signal intensity over an ROI  $B$ , centered at point  $\mathbf{s}$ , as follows:

$$\begin{aligned}
F_B(\mathbf{s}) &\propto \sum_{\mathbf{k}_j \in A} f(\mathbf{k}_j) \overline{p(\mathbf{k}_j)} e^{i2\pi(\mathbf{s}, \mathbf{k}_j)} \\
&= \sum_{\mathbf{k}_j \in A} \left( \int_{\Omega} F(\mathbf{u}) e^{-i2\pi(\mathbf{u}, \mathbf{k}_j)} d\mathbf{u} \right) \overline{p(\mathbf{k}_j)} e^{i2\pi(\mathbf{s}, \mathbf{k}_j)} \\
&= \int_{\Omega} F(\mathbf{u}) \sum_{\mathbf{k}_j \in A} \overline{p(\mathbf{k}_j)} e^{i2\pi(\mathbf{s}-\mathbf{u}, \mathbf{k}_j)} d\mathbf{u} \\
&= \int_{\Omega} F(\mathbf{u}) P(\mathbf{s} - \mathbf{u}), \tag{17}
\end{aligned}$$

where

$$P(\mathbf{x}) = \sum_{\mathbf{k}_j \in A} \overline{p(\mathbf{k}_j)} e^{i2\pi(\mathbf{x}, \mathbf{k}_j)}. \tag{18}$$

Hence the integral of signal intensity over  $B$  will be approximately equal to the image convolved with a point spread function which depends on the function  $p$ . By controlling the shape of  $P$  we can control the point-spread function and minimize signal leakage outside of the ROI. Ideally we would like  $P(\mathbf{x})$  to be completely concentrated on a region of the same size and shape as  $B$ . When  $k$ -space is sampled on a Cartesian grid,  $P(\mathbf{x}) = G(\mathbf{x})$ , which is the filter covered in previous papers and summarized in section I. In the non-uniform case  $P(\mathbf{x})$  will take a different form and the calculation of the PSWF function needs to be altered accordingly.

#### IV. Determining the generalized prolate spheroidal wave function

In this section we derive the optimal filter for the case when  $k$ -space is sampled non-uniformly and image-space is chosen to be discrete (Fig. 1a). The continuous image-space case is discussed briefly at the end of the section. In the PSWF theory, we are interested in finding the function  $P$  that solves the following optimization problem:

$$\lambda = \max_{p(\mathbf{k})} \frac{\sum_{\mathbf{x}_i \in B} |P(\mathbf{x}_i)|^2}{\sum_{\mathbf{x}_i \in \Omega} |P(\mathbf{x}_i)|^2} \quad (19)$$

where  $P(\mathbf{x})$  is defined in (18).

Let  $\Omega$  denote the set of  $N^2$  points in an  $N \times N$  image-space, and let  $B$  consist of  $b$  adjacent voxels that cover the chosen shape of the ROI. To present the problem in matrix notation, let  $\mathbf{F}$  represent the vector form of  $F(\mathbf{x})$ , for  $\mathbf{x} \in \Omega$ . Similarly, let  $\mathbf{p}$  and  $\mathbf{f}$  be vectors of  $p(\mathbf{k})$  and  $f(\mathbf{k})$ , respectively, for  $\mathbf{k} \in A$ . We will also make use of the inner product notation, where

$$(\mathbf{F}, \mathbf{G})_{\Omega} = \sum_{\mathbf{x} \in \Omega} F(\mathbf{x}) \overline{G(\mathbf{x})}. \quad (20)$$

Further let us define two operators,

$$\mathbf{T}\mathbf{F} = \sum_{\mathbf{x} \in \Omega} e^{-i\frac{2\pi}{N}(\mathbf{x}, \mathbf{k}_j)} F(\mathbf{x}) \quad (21)$$

and

$$\mathbf{T}^*\mathbf{f} = \sum_{\mathbf{k}_j \in A} e^{i\frac{2\pi}{N}(\mathbf{x}, \mathbf{k}_j)} f(\mathbf{k}_j) \quad (22)$$

Here it should be noted that  $\mathbf{T}$  is an  $a \times N^2$  and  $\mathbf{T}^*$  an  $N^2 \times a$  matrix. It is important to note two useful facts about the operators  $\mathbf{T}$  and  $\mathbf{T}^*$ . First,

$$\begin{aligned}
(\mathbf{T}\mathbf{f}, \mathbf{p})_A &= \sum_{\mathbf{k}_j \in A} \sum_{\mathbf{x} \in \Omega} e^{-i\frac{2\pi}{N}(\mathbf{x}, \mathbf{k}_j)} f(\mathbf{x}) \overline{p(\mathbf{k}_j)} \\
&= \sum_{\mathbf{x} \in \Omega} f(\mathbf{x}) \sum_{\mathbf{k}_j \in A} \overline{e^{i\frac{2\pi}{N}(\mathbf{x}, \mathbf{k}_j)} p(\mathbf{k}_j)} \\
&= (\mathbf{f}, \mathbf{T}^* \mathbf{p})_\Omega
\end{aligned} \tag{23}$$

and similarly,

$$(\mathbf{T}^* \mathbf{p}, \mathbf{f})_\Omega = (\mathbf{p}, \mathbf{T}\mathbf{f})_A. \tag{24}$$

Additionally, the matrix  $\mathbf{I}_B \mathbf{T}^*$  is defined as the  $b$  rows of the matrix  $\mathbf{T}^*$  that correspond with elements in the ROI  $B$  and similarly,  $\mathbf{T}\mathbf{I}_B$  will consist of the  $b$  columns of the matrix  $\mathbf{T}$  that correspond with elements in  $B$ . When multiplying these two matrices we will simply write  $\mathbf{T}\mathbf{I}_B \mathbf{T}^*$ , instead of  $\mathbf{T}\mathbf{I}_B \mathbf{I}_B \mathbf{T}^*$ .

Turning our attention back to (19), for any fixed  $B \subset \Omega$ , we can rewrite the numerator, in discrete form, as follows:

$$\begin{aligned}
\sum_{\mathbf{x}_i \in B} |P(\mathbf{x}_i)|^2 &= \sum_{\mathbf{x}_i \in B} P(\mathbf{x}_i) \overline{P(\mathbf{x}_i)} \\
&= \sum_{\mathbf{x}_i \in B} \sum_{\mathbf{k}_j \in A} e^{i\frac{2\pi}{N}(\mathbf{x}_i, \mathbf{k}_j)} p(\mathbf{k}_j) \sum_{\mathbf{k}_j \in A} \overline{e^{i\frac{2\pi}{N}(\mathbf{x}_i, \mathbf{k}_j)} p(\mathbf{k}_j)} \\
&= \sum_{\mathbf{x}_i \in B} (\mathbf{T}^* \mathbf{p})(\mathbf{x}_i) \overline{(\mathbf{T}^* \mathbf{p})(\mathbf{x}_i)} \\
&= (\mathbf{I}_B \mathbf{T}^* \mathbf{p}, \mathbf{I}_B \mathbf{T}^* \mathbf{p})_\Omega \\
&= (\mathbf{p}, \mathbf{T}\mathbf{I}_B \mathbf{T}^* \mathbf{p})_A.
\end{aligned} \tag{25}$$

Similarly we can rewrite the denominator as,

$$\sum_{\mathbf{x}_i \in B} |P(\mathbf{x}_i)|^2 = (\mathbf{p}, \mathbf{T}\mathbf{T}^* \mathbf{p})_A. \quad (26)$$

Let us define  $\mathbf{R}=(\mathbf{T}\mathbf{T}^*)^{1/2}$ . Since  $\mathbf{R}^*=\mathbf{R}$ , it holds that  $(\mathbf{p}, \mathbf{R}\mathbf{R}\mathbf{p})_A = (\mathbf{R}\mathbf{p}, \mathbf{R}\mathbf{p})_A$ .

Let  $\xi = \mathbf{R}\mathbf{p}$ . Now (25) can be written as,

$$\begin{aligned} (\mathbf{p}, \mathbf{T}\mathbf{I}_B \mathbf{T}^* \mathbf{p})_A &= (\mathbf{R}^{-1}\xi, \mathbf{T}\mathbf{I}_B \mathbf{T}^* \mathbf{R}^{-1}\xi) \\ &= (\xi, \mathbf{R}^{-1}\mathbf{T}\mathbf{I}_B \mathbf{T}^* \mathbf{R}^{-1}\xi)_A \end{aligned} \quad (27)$$

and the problem defined in (19) can be reformulated as follows:

$$\begin{aligned} &\max (\xi, \mathbf{R}^{-1}\mathbf{T}\mathbf{I}_B \mathbf{T}^* \mathbf{R}^{-1}\xi)_A \\ &\text{subject to } (\xi, \xi)_A = 1 \end{aligned} \quad (28)$$

The solution to this problem is the largest eigenvalue  $\lambda$  and the corresponding eigenvector  $\xi$  of the matrix  $\mathbf{K}_{A,B} = \mathbf{R}^{-1}\mathbf{T}\mathbf{I}_B \mathbf{T}^* \mathbf{R}^{-1}$ . In the case when k-space is sampled uniformly,  $\mathbf{R}^2 = \mathbf{T}\mathbf{T}^* = \mathbf{I}$ , where  $\mathbf{I}$  is the  $a \times a$  identity matrix, and  $\mathbf{K}_{A,B}$  can be written as:

$$\mathbf{K}_{A,B} = \mathbf{R}^{-1}\mathbf{T}\mathbf{I}_B \mathbf{T}^* \mathbf{R}^{-1} = \mathbf{T}\mathbf{I}_B \mathbf{T}^*. \quad (29)$$

Hence, for each  $\mathbf{k}, \mathbf{k}' \in A$ ,

$$K_{A,B}(\mathbf{k}, \mathbf{k}') = \frac{1}{N^2} \sum_{\mathbf{x} \in B} \exp\left\{-\frac{2\pi i}{N}(\mathbf{x}, \mathbf{k} - \mathbf{k}')\right\} \quad (30)$$

which is the kernel shown in (7). However, when k-space is sampled non-uniformly we have to take the matrix  $\mathbf{R}$  into consideration in our continued calculations.

Since  $\lambda$  is the largest eigenvalue of  $\mathbf{K}_{A,B}$  and  $\xi$  its corresponding eigenvector, it must hold that

$$\lambda\xi = \mathbf{R}^{-1}\mathbf{T}\mathbf{I}_B\mathbf{T}^*\mathbf{R}^{-1}\xi. \quad (31)$$

In general,  $b \ll a$ , and hence, to simplify the calculation,  $\mathbf{K}_{A,B}$  can be expressed in image-space to reduce the matrix size. Let  $\eta = \mathbf{I}_B\mathbf{T}^*\mathbf{R}^{-1}\xi$ . Multiplying both sides of (31) by the matrix  $\mathbf{I}_B\mathbf{T}^*\mathbf{R}^{-1}$  yields

$$\begin{aligned} \lambda\eta &= \mathbf{I}_B\mathbf{T}^*\mathbf{R}^{-1}\mathbf{R}^{-1}\mathbf{T}\mathbf{I}_B\mathbf{T}^*\mathbf{R}^{-1}\xi \\ &= \mathbf{I}_B\mathbf{T}^*\mathbf{R}^{-2}\mathbf{T}\mathbf{I}_B\eta \\ &= \mathbf{K}_{B,A}\eta \end{aligned} \quad (32)$$

This shows that  $\eta$  is an eigenvector of the matrix  $\mathbf{K}_{B,A}$ , which is a  $b \times b$  matrix that has the same largest eigenvalue,  $\lambda$ , as  $\mathbf{K}_{A,B}$ . Once  $\eta$  is obtained, we can use it to calculate the optimal filter  $\mathbf{p}$ . Begin by multiplying both sides of the equation  $\eta = \mathbf{I}_B\mathbf{T}^*\mathbf{R}^{-1}\xi$  with the matrix  $\mathbf{R}^{-1}\mathbf{T}\mathbf{I}_B$ . Together with (31) this gives the following relationship between  $\eta$  and  $\xi$ :

$$\mathbf{R}^{-1}\mathbf{T}\mathbf{I}_B\eta = \mathbf{R}^{-1}\mathbf{T}\mathbf{I}_B\mathbf{T}^*\mathbf{R}^{-1}\xi = \lambda\xi. \quad (33)$$

This in turn implies that

$$\xi = \frac{1}{\lambda}\mathbf{R}^{-1}\mathbf{T}\mathbf{I}_B\eta. \quad (34)$$

Using this relationship, and the fact that  $\xi = \mathbf{R}\mathbf{p}$ , we can express  $\mathbf{p}$  as,

$$\mathbf{p} = \mathbf{R}^{-1}\xi = \frac{1}{\lambda}\mathbf{R}^{-2}\mathbf{T}\mathbf{I}_B\boldsymbol{\eta} \quad (35)$$

The inverse Fourier transform of  $\mathbf{p}$  is the function for which the ratio in (19) is maximized and therefore maximizes the energy over the predefined ROI  $B$ . Equation (35) represents the optimal PSWF filter for the ROI  $B$  and  $P(\mathbf{x}_i) = (\mathbf{T}\mathbf{p})(\mathbf{x}_i)$  represents the corresponding point spread function.

Once  $\mathbf{p}$  is obtained, the total signal intensity over the ROI  $B$  can be evaluated directly from the reduced k-space area using the formula:

$$\sum_{x \in B} F(x) \propto \sum_{\mathbf{k}_j \in A} f(\mathbf{k}_j) \overline{p(\mathbf{k}_j)} \quad (36)$$

as shown by (17).

In this section image-space was chosen to be discrete. It should be noted that the problem can be set up in an analogous manner for continuous image-space. However, we ultimately determined that treating image-space as discrete allowed for a simpler expression of the dual kernel in image-space (32), which in turn greatly simplifies numerical calculation.

## V. Calculation of the generalized PSWF

The main difficulty in applying this method to MRI data, is inverting the matrix  $\mathbf{R}^2$ . In certain situations, this can be difficult due to the size of the matrix and to the fact that the smallest eigenvalues can take values close to 0, making the matrix ill-conditioned. When this scenario arises there are two potential problems in calculating  $\mathbf{p}$ . The first difficulty is the calculation of the kernel  $\mathbf{K}_{B,A}$  and the corresponding

largest eigenfunction  $\boldsymbol{\eta}$ . The second difficulty is the calculation of  $\mathbf{R}^{-2}\mathbf{T}\mathbf{I}_B\boldsymbol{\eta}$ . The first problem can be solved by substituting  $\mathbf{R}^{-2}=(\mathbf{T}\mathbf{T}^*)^{-1}$  with the pseudoinverse of  $\mathbf{T}\mathbf{T}^*$ .

When calculating the kernel  $\mathbf{K}_{B,A}$  we can avoid the problem of inverting  $\mathbf{R}^2$  by defining a mapping. Let  $\mathbf{U}: \mathbf{R}\mathbf{k} \rightarrow \mathbf{T}^*\mathbf{k}$ , where  $\mathbf{U} = (\mathbf{u}_1, \dots, \mathbf{u}_a)$  and  $\mathbf{u}_1, \dots, \mathbf{u}_a \in \Omega$ . The vectors  $\mathbf{u}_i$  form an orthogonal basis of  $\Omega$ . We can write  $\mathbf{T}^*$  and  $\mathbf{T}$  in terms of the unitary matrix  $\mathbf{U}$  as follows:  $\mathbf{T}^* = \mathbf{U}\mathbf{R}$  and  $\mathbf{T} = \mathbf{R}\mathbf{U}^{-1}$ .

Since  $\mathbf{R}=(\mathbf{T}\mathbf{T}^*)^{1/2}=\mathbf{R}^*$  and  $\|\mathbf{U}\boldsymbol{\varepsilon}\| = \|\boldsymbol{\varepsilon}\|$ , the matrix  $\mathbf{U}\mathbf{U}^{-1}$  will be the projection onto the range of  $\mathbf{T}^*$ . We can rewrite the generalized prolate kernel,  $\mathbf{K}_{B,A}$ , in terms of the matrices  $\mathbf{U}$  and  $\mathbf{U}^{-1}$ ,

$$\begin{aligned}\mathbf{K}_{B,A} &= \mathbf{I}_B \mathbf{T}^* \mathbf{R}^{-2} \mathbf{T} \mathbf{I}_B \\ &= \mathbf{I}_B \mathbf{U} \mathbf{U}^{-1} \mathbf{I}_B\end{aligned}\tag{37}$$

Using this mapping we can calculate the kernel without having to invert the matrix  $\mathbf{R}^2$ . Instead we need to find a basis which spans  $\mathbf{T}^*$ . This can be done in a variety of fashions, for example by calculating the singular value decomposition of  $\mathbf{T}^*$ . Once we have determined  $\mathbf{U}$ , it is easy to calculate  $\mathbf{K}_{B,A}$  and obtain the largest eigenfunction in the usual manner.

As the matrix  $\mathbf{R}^{-2}$  works as a weighing function that compensates for the non-uniform sampling, an alternative approximate solution that is significantly less computer intensive is to substitute the matrix  $\mathbf{R}^{-2}$  with a matrix with diagonal elements equal to the values of some density compensation function. This will give a reasonable approximation at a fraction of the cost for most sampling trajectories that one would potentially use in MRI.

## METHODS

The generalized 2D-PSWF method was implemented in Matlab (Mathworks Inc.) on a personal computer. To demonstrate its utility for dynamic studies, a high temporal resolution fMRI experiment was designed to simultaneously track the hemodynamic signals in both visual and motor cortices while the subject undergoes a visual-motor activation paradigm. Following the steps of the generalized 2D-

PSWF method, circular ROIs with a radius of 8 mm were chosen for the primary visual cortex and the primary motor cortex (Fig. 8). Since the ROIs were chosen to be circles, the optimal sampling in k-space was also circular [10]. This predetermined circular sub-region of k-space was sampled with 3628 points using a spiral trajectory [19] that allowed a minimum repetition time of 60 ms (Fig. 9). After calculating the optimal filter  $\mathbf{p}$  corresponding to this choice of  $A$  and  $B$ , the signal intensity over the circular ROI,  $B$ , was calculated with the acquired k-space data using (36).

The activation paradigm consisted of six cycles of 30 s intervals. At the beginning of each interval a 100 ms light flash was presented. The subject was instructed to press a button with their right thumb immediately after sensing the flash, thereby leading to activation of the motor cortex. During the 30 second interval, 500 images were acquired rapidly every 60 ms. The sequence was repeated six times, each time producing a dynamic data set of 500 temporal points. The images were obtained in an oblique slice containing both primary visual and motor cortices using a spiral trajectory. The dynamic signals from the pre-determined ROIs were acquired with an effective TE 30 ms, flip angle 15 degrees, field of view  $240 \times 240$  mm<sup>2</sup>, slice thickness 10.3 mm, matrix  $24 \times 24$  and bandwidth 12.5 kHz. The experiment was performed on a 3.0 T whole body scanner (GE magnet, General Electric Medical Systems, Milwaukee, WI, USA). A healthy male volunteer (age 28) participated in the study after giving written informed consent. The activated ROIs in the slice were determined by correlating their time-course signal intensity with the experimental paradigm. For comparison purposes, the acquired k-space data were also used to reconstruct low-resolution images using conventional re-gridding methods [20] for the dynamic analysis.

## RESULTS

In this section, a computer experiment is described to illustrate the concepts and mathematical procedure of the generalized 2D-PSWF method for non-uniformly sampled data. An application of the method to fMRI is demonstrated using experimental data.

## I. A Computer Phantom Study

As shown in Fig. 3, we constructed a  $64 \times 64$  phantom image containing an ellipse representing a human brain that consists of 1209 points. The image intensities are assigned values of 1 or 0 for the points inside or outside the ellipse, respectively. Two smaller ellipses having an intensity of 1.1, each consisting of 75 points, are placed inside the larger ellipse to simulate ROIs with static contrast to the large ellipse. To simulate a dynamic image series, this base image is recreated 64 times according to a boxcar paradigm consisting of eight cycles of four “ON” and four “OFF” periods. An image is considered in the “ON” state, if there is an “activated” circular ROI with intensity 1.05 in the corner of the large ellipse. Conversely, an image is considered in the “OFF” state, if no such ROI exists in the image. The “activated” ROI consists of 21 points. A 5% white noise floor is added to all 64 images. These dynamic images are subsequently transformed into k-space for application of the 2D-PSWF method to measure the dynamic signal change in a given ROI,  $B$ .

## II. Choosing $A$ and $B$

In this simulation, our ROI  $B$  is chosen to be the same size and shape as the “activated” circular region consisting of 21 points. The optimal k-space sampling area,  $A$ , corresponding to this ROI will also be circular [10]. The spiral sampling trajectory is the natural choice for sampling a circular k-space region  $A$ . In order to demonstrate the influence of the size of  $A$ , three sampling sizes shown in Fig. 4 are given. Our first choice of  $A$  (Fig. 4a) consists of 454 points and covers approximately 11% of the total area of k-space needed for a full image reconstruction of a  $64 \times 64$  image. We also choose two other sampling regions for comparison, one that consists of 910 points covering 17% of k-space (Fig. 4b) and another that consists of 3664 points covering 78.5% of k-space (Fig. 4c).

## III. Eigenvalues and eigenvectors

Using the generalized prolate kernel in (32), the optimal filter,  $p(\mathbf{k})$ , with respect to  $A$  and  $B$  can be calculated. Fig. 5 shows the optimal filter functions corresponding to the three different sampling sizes.

The signal leakage for each of the three filters is shown in Fig. 6. It is clear that as the sampling size  $A$  increases, so does the concentration of the signal within the ROI.

In the rectilinear case [8]-[9] a lower limit for choosing the number of sampling points was given by the relationship

$$a = 3N^2/b, \quad (38)$$

where  $b$  is the size of the ROI  $B$  and  $N^2$  is the size of the image. This formula cannot be directly applied to non-uniform data, as the area of k-space effectively covered is more important than the actual number of points sampled. However, by calculating the lower limit for  $a$  in the rectilinear case according to (38), we can determine the appropriate area of the k-space region that needs to be covered. For  $b$  equal to 21 and  $N$  equal to 64, we find that we would need to sample 585 points in the rectilinear case. This corresponds to a circular region of k-space with radius 14 unit points. It is interesting to note that the first sampling region is smaller than this heuristic threshold, while the latter two lie above it.

#### IV. Calculating the signal intensity over $B$

Once the filter  $p(\mathbf{k})$  corresponding to the given k-space subset  $A$  is obtained, the total signal intensity over  $B$  can be calculated directly from the reduced k-space area using (36). In this study the 2D-PSWF method was applied to data sampled using the sampling trajectory with 910 points in Fig. 4b. Fig. 7 shows a plot (solid line) of  $\sum_{\mathbf{x} \in B} F(\mathbf{x}, t)$  as a function of the image number,  $t$ , obtained using a reduced k-space sample and the 2D-PSWF method. Also contained in the same figure is a plot of dynamic signal change over  $B$  (dotted line), obtained by taking the sum over  $B$  directly from the phantom images. It is clear that with the 2D-PSWF method the signal intensity over  $B$  closely follows the true signal change even though only 17% of k-space was used in the analysis.

#### V. Application to experimental data

To validate the theoretical analysis and computer modeling results, the utility of the generalized 2D-PSWF method for dynamic studies was tested experimentally using a visual-motor stimulation fMRI paradigm. With the generalized 2D-PSWF method, the dynamic signal change over each of the two ROIs during the execution of the stimulation paradigm was obtained. Fig. 10 shows a plot of the average signal intensity in the visual cortex (bold line) and the motor cortex (light line) over the six runs. A clear delay in motor activation due to reaction time can be seen. With the increased temporal resolution and SNR, we can more precisely determine the delay time in motor activation to be approximately 300 *ms*. For both cortices, the ‘negative dip’ in the time-course plot can be seen clearly. Fig. 11 shows a similar plot obtained from the same ROIs using images reconstructed with conventional re-gridding methods. The motor activation is significantly attenuated as a result of partial volume effects.

The generalized 2D-PSWF methodology was able to detect the signal change in both activated regions of the brain. By translating the filter, the signal intensity over other circular ROIs centered at different areas of the brain could be calculated. No other significant activation was consistently detected in other regions in the chosen slice.

## **DISCUSSION**

This paper presents a generalization of the 2D-PSWF method to non-uniformly sampled k-space data. This generalization is important, as k-space is typically sampled in a non-rectilinear fashion for dynamic MRI studies due to hardware limitations. The example presented here samples k-space with a smooth spiral trajectory that eliminates abrupt switching of spatial encoding gradients. This approach is also advantageous for implementation of the 2D-PSWF method because it is more straightforward to sample the tailored non-square k-space regions using a spiral trajectory rather than using conventional rectilinear k-space sampling methods.

From a practical point of view, the major difficulty in applying the 2D-PSWF method to MR data is the computational difficulties that are involved in inverting the matrix  $\mathbf{R}^2$ . For typical MRI sampling trajectories, the matrix is often ill-conditioned because the smallest eigenvalues take values close to 0. In

these situations, one can substitute the inverse with the pseudo-inverse that is a generalization of matrix inversion that can be computed using singular value decomposition. An additional difficulty is that when  $\mathbf{R}^2$  is large, the calculation of the inverse or pseudo-inverse is computationally intensive. An alternative approximate solution that is significantly less computationally intensive is to substitute a matrix having diagonal elements equal to some density compensation weight  $w(\mathbf{k})$  for the matrix  $\mathbf{R}^2$ . This will give a reasonable approximation at a fraction of the cost for most sampling trajectories used in MRI.

In the 2D-PSWF method, the reduction of k-space sampling is realized by trading off spatial resolution for temporal resolution while maintaining high SNR. Tailoring the sampling region and matching the 2D-PSWF filter to the shape and size of a given ROI allow us to optimize the reduction of k-space sampling with minimal truncation penalty. The non-square shaped ROI reduces the signal leakage outside of the ROI, which improves the contrast-to-noise ratio (CNR). As demonstrated in Fig. 10, the improved temporal resolution provides more detailed information about hemodynamic signals of visual and motor cortices. A ‘negative dip’ that peaks 2s after the onset of visual stimulation, is clearly visible in the hemodynamic signals from both visual and motor cortices. Since the amplitude of the negative dip is much smaller than the positive BOLD effect ( $< 1\%$  at 3T), similar results reported previously generally required signal averaging across multiple runs from multiple subjects [21]. With the generalized PSWF method, the time course signal from the visual cortex allows the data to reliably characterize the hemodynamic response from a single subject. This is important for the clinical applications where diagnoses of abnormalities are normally based on a single subject study. The corresponding negative dip for the motor cortex is apparent but less pronounced in the plot. This may be due to averaging effect of the temporal signals over all the runs because the time of subject responding to the visual stimulation can be different with each run. With the conventional gridding method, both positive and negative activations in the time-course plot for motor cortex are diminished.

The other advantage of the high temporal resolution provided by the PSWF method is the increased frequency-domain bandwidth of the dynamic signal. This allows for better identification and subsequent filtering of undesirable physiologic noises in the hemodynamic signal. As shown in Fig. 11, the

characteristics for the signal over the motor cortex were interfered by a periodic modulation in the time course signal. This can be easily identified in the Fourier transform of the temporal signals shown in Fig. 12, and subsequently removed by a specific bandpass filter.

Typically under the conditions needed to increase the temporal resolution, tracking the hemodynamic responses is difficult because the image SNR is significantly attenuated by the drastically reduced TR. However, as seen in Fig. 10, the 2D-PSWF method provides an adequate SNR for high temporal resolution dynamic studies. Thus, the 2D-PSWF method can be a valuable tool for the studies of dynamics of the brain function such as functional neuron-neuron interaction, synchronization and connectivity [22]-[24].

## **CONCLUSIONS**

The 2D-PSWF method addresses issues inherent in the fast Fourier transform, such as partial volume effects due to the square-shaped voxel and the inverse relationship between image resolution and k-space sampling area (temporal resolution). These problems are frequently encountered in rapid imaging and chemical shift imaging. This method uses prior knowledge of a given ROI and the temporal resolution requirements to design a reduced sampling area of k-space with a matched 2D-PSWF filter, such that optimal SNR and minimal truncation artifacts are achieved.

This paper introduces a generalized version of the 2D-PSWF method that allows its application to non-uniformly sampled k-space data with arbitrary trajectory. This extension is important; as the k-space sub-regions normally take a non-square shape when applying the 2D-PSWF method and sampling on the Cartesian grid for a non-square k-space is inefficient. To validate our method, the generalized 2D-PSWF method was applied to a high temporal resolution fMRI study using a spiral sampling trajectory and its effectiveness in tracking the dynamic signal change over the visual and motor cortices was illustrated.

## **REFERENCES**

1. S. Ogawa, D. W. Tank, R. Menon, J. M. Ellermann, S. G. Kim, H. Merkle, and K. Ugurbil, "Intrinsic Signal Changes Accompanying Sensory Stimulation: Functional Brain Mapping with Magnetic Resonance Imaging", *Proc. Natl. Acad. Sci. USA*, Vol. 89, pp. 5951-5955, 1992.
2. K. K. Kwong, J. W. Belliveau, D. A. Chesler, I. E. Goldberg, R. M. Weisskoff, B. P. Poncelet, D. N. Kennedy, B. E. Hoppel, M. S. Cohen, R. Turner, H. M. Cheng, T. J. Brady, and B. R. Rosen, "Dynamic Magnetic Resonance Imaging of Human Brain Activity During Primary Sensory Stimulation", *Proc. Natl. Acad. Sci. USA*, Vol. 89, pp. 5675-5679, 1992.
3. T. Ernst and J. Hennig, "Observation of a Fast Response in Functional MR", *Magn. Reson. Med.*, Vol. 32, pp. 146-149, 1994.
4. J. Hennig, C. Janz, O. Speck, and T. Ernst, "Functional Spectroscopy of Brain Activation Following a Single Light Pulse: Examination of the Mechanism of the Fast Initial Response", *Int. J. Imaging Syst. Technol.*, Vol. 6, pp. 203-208, 1995.
5. X. Hu, T. H. Le, and K. Ugurbil, "Evaluation of the Early Response in fMRI in Individual Subjects Using Short Stimulus Duration", *Magn. Reson. Med.*, Vol. 37, pp. 877-884, 1997.
6. B. Biswal, F. Z. Yetkin, V. M. Haughton, and J. S. Hyde, "Functional Connectivity in the Motor Cortex of Resting Human Brain Using Echo-Planar MRI", *Magn. Reson. Med.*, Vol. 34, pp. 537-541, 1995.
7. K. Hendrich, X. Hu, R. S. Menon, H. Merkle, P. Camarata, R. Heros, and K. Ugurbil, "Spectroscopic Imaging of Circular Voxels with a Two-Dimensional Fourier-Series Window Technique", *J. Magn. Reson. Series B*, Vol. 105, pp. 225-232, 1994.
8. L. Shepp, and C. H. Zhang, "Fast Functional Magnetic Resonance Imaging via Prolate Wavelets", *Applied and Computational Harmonic Analysis*, Vol. 9, pp. 99-119, 2000.
9. Q. X. Yang, M. Lindquist, L. Shepp, C. H. Zhang, J. Wang, and M. B. Smith, "Two Dimensional Prolate Spheroidal Wave Functions for MRI", *J. Magn. Reson.*, Vol. 158, pp. 43-51, 2002.
10. M. Lindquist, "Optimal Data Acquisition in fMRI using Prolate Spheroidal Wave Functions", *Int. J. Imaging Syst. Technol.*, Vol. 13, pp. 803-812, 2003.

11. Q. X. Yang, L. Shepp, C. H. Zhang, R. J. Demeure, and M. B. Smith, "A New Algorithm of Optimal Data Acquisition and Reconstruction for Non-Square Voxel", in *Proceedings of the 7th ISMRM Annual Meeting*, Philadelphia, p. 665, 1999.
12. M. Lindquist, Q. X. Yang, C. H. Zhang, R. J. Demeure, M. B. Smith, and L. Shepp, "ROI Tailored k-Space Sampling and a 2D Prolate Spheroidal Wave Function Filter: Reduction of Spectral Contamination in Spectroscopic Imaging", in *Proceedings of the 8th ISMRM Annual Meeting*, Denver, p. 1842, 2000.
13. D. Slepian and H. O. Pollak, "Prolate Spheroidal Wave Functions, Fourier Analysis and Uncertainty, I", *Bell System Tech. J.*, Vol. 40, pp. 43-64, 1961.
14. H. J. Landau and H. O. Pollak, "Prolate Spheroidal Wave Functions, Fourier Analysis and Uncertainty, II", *Bell System Tech. J.*, Vol. 40, pp. 65-84, 1961.
15. H. J. Landau and H. O. Pollak, "Prolate Spheroidal Wave Functions, Fourier Analysis and Uncertainty, III", *Bell System Tech. J.*, Vol. 41, pp. 1295-1336, 1962.
16. D. Slepian, "Prolate Spheroidal Wave Functions, Fourier Analysis and Uncertainty – V: The discrete case", *Bell System Tech. J.*, Vol. 57, no. 5, pp. 1371-1420, 1978.
17. J.M.Varah, "The prolate matrix", *SIAM J. Linear Alg. Applicat.*, no. 187, p. 269-278, 1993.
18. D. B. Percival and A. T. Walden, *Spectral Analysis for Physical Applications*, Cambridge University Press, Cambridge, UK, 1993.
19. G. H. Glover, "Simple Analytic Spiral K-Space Algorithm", *Magn. Reson. Med.*, Vol. 42, pp. 412-415, 1999.
20. J. Jackson, C. Meyer, D. Nishimura and A. Macovski, "Selection of a convolution function for Fourier inversion using gridding", *IEEE Transactions on Medical Imaging*, Vol. 10, pp. 473-478, 1991.
21. E. Yacoub, A. Shmuel, J. Pfeuffer, P-F Moortele, G. Adriany, K. Ugurbil, X. Hu, "Investigation of the Initial Dip at 7 Tesla", *NMR in Biomed.*, Vol. 14, pp. 408-412, 2001.

22. B. Biswal, F.Z. Yetkin, V.M. Haughton, J.S. Hyde, "Functional connectivity in the motor cortex of resting human brain using echo-planar MRI", *Magn. Reson. Med.*, Vol. 34, pp. 537-541, 1995.
23. C. Buchel and K.J. Friston, "Modulation of connectivity in visual pathways by attention: Cortical interactions evaluated with structural equation modelling and fMRI", *Cerebral Cortex*, Vol. 7, pp. 768-778, 1997.
24. A.R. McIntosh, F.L. Bookstein, J.V. Haxby, C.L. Grady, "Spatial pattern analysis of functional brain images using partial least squares", *NeuroImage*, Vol. 3, pp. 143-157, 1996.

## FIGURES

Fig. 1: (a) Discrete/Discrete case - k-space consists of discrete measurements made inside of the region  $A$ . Image-space consists of the  $N^2$  voxel elements contained in the  $N \times N$  image.  $B$  consists of a set of voxels. (b) Discrete/Continuous case - Image-space has support  $\Omega$ .

Fig. 2: The two largest eigenvalues for the case when  $B$  is a small circular region with fixed radius (radius =  $7.5mm$ , FOV =  $200mm$ ) and  $A$  is a circular region with variable radius, containing  $a$  equally spaced k-space measurements. As  $a$  increases both eigenvalues approach 1. The appropriate size of  $A$  is when the largest eigenvalue is equal to one and the second largest is significantly below 1.

Fig. 3: Computer phantom images. (a) Image without activation. (b) Image with activation in  $B$ . (c) Image with activation in  $B$  and 5% white noise.

Fig. 4: Spiral sampling trajectories consisting of (a) 454 points, (b) 910 points and (c) 3664 points.

Fig 5: The optimal filter function,  $\mathbf{p}$ , corresponding to each of the three sampling schemes shown in Fig. 4. The x-axis represents each point in the order it was sampled.

Fig. 6: The function  $P(\mathbf{x})$  and the corresponding signal leakage given by each of the three filters shown in Fig. 5.

Fig. 7: The time-course signal intensities over  $B$  using the 2D-PSWF method and only 17% of k-space. The signal intensity with full k-space sampling is plotted in dotted lines for comparison.

Fig. 8: The two ROIs (21 voxels) in the motor (upper) and visual (lower) cortices superimposed on a low-resolution image of the acquired slice.

Fig. 9: The optimal sampling region corresponding to the ROIs given in Fig 6. The trajectory used in the experiment is superimposed. Compare this with full k-space (64×64) which is marked by the black box.

Fig. 10: The dynamic signal change over the visual (bold) and motor (light) cortex for the first 18s following visual stimuli. The delay in time-to-peak between the two curves is approximately 300 ms.

Fig. 11: The dynamic signal changes over the visual (bold) and motor (light) cortex for the first 18s following visual stimuli, obtained by integrating the signal over the ROIs in images reconstructed using re-gridding methods.

Fig. 12: The Fourier transform of the dynamic signal over the motor cortex shown in Fig. 9. A peak at  $\omega=16$  indicates the frequency of the periodic fluctuation apparent in the signal.

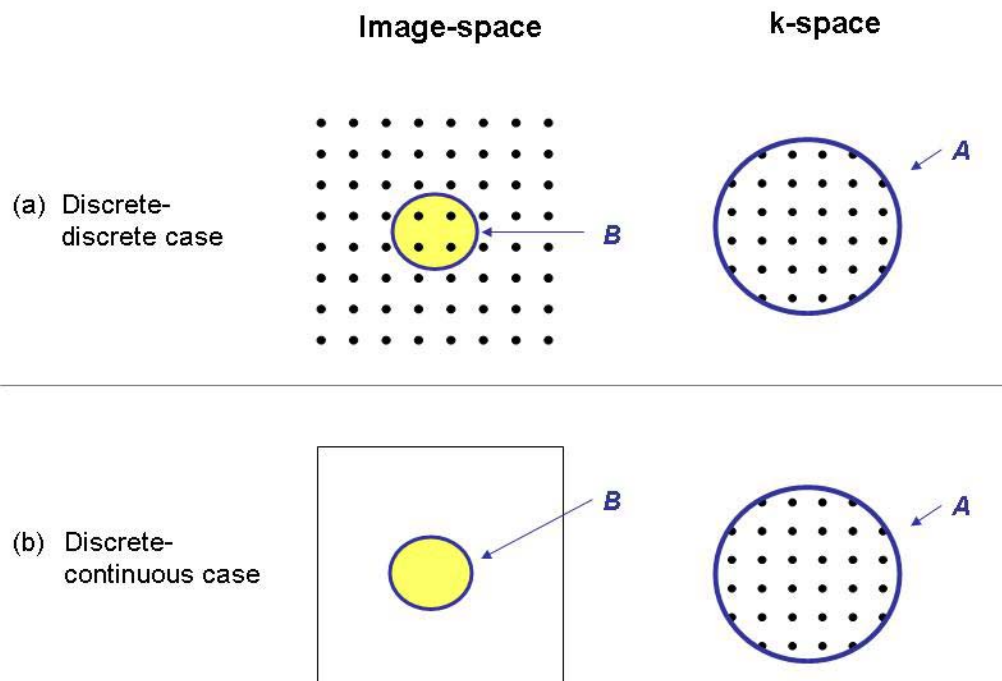


Fig. 1

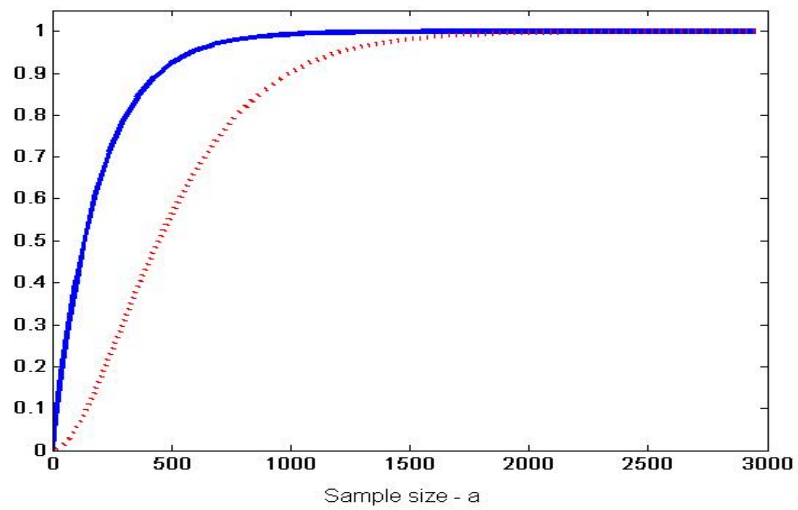


Fig. 2

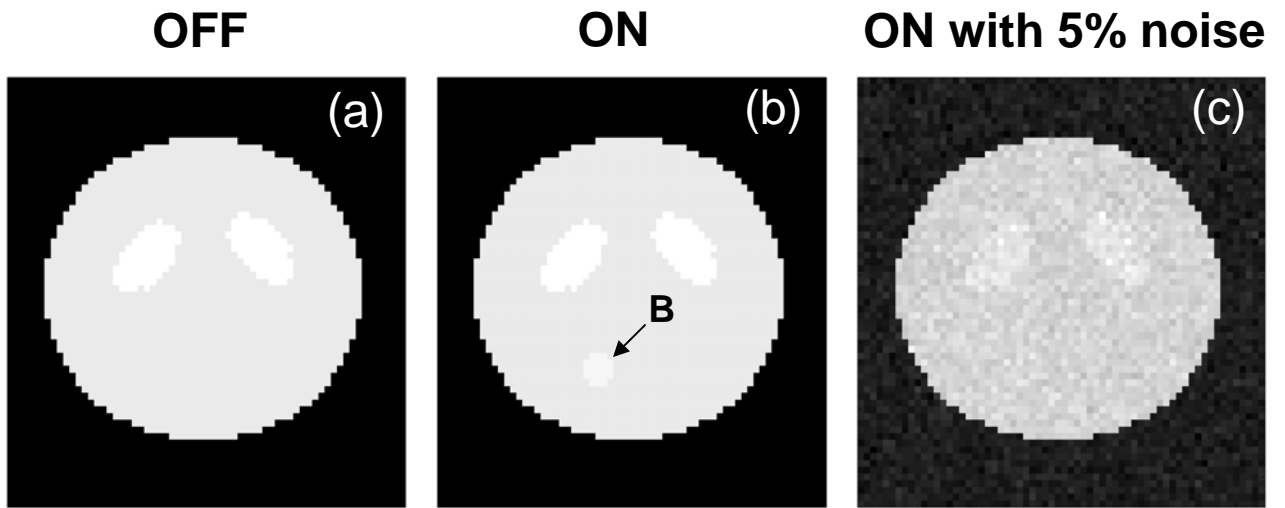


Fig 3.

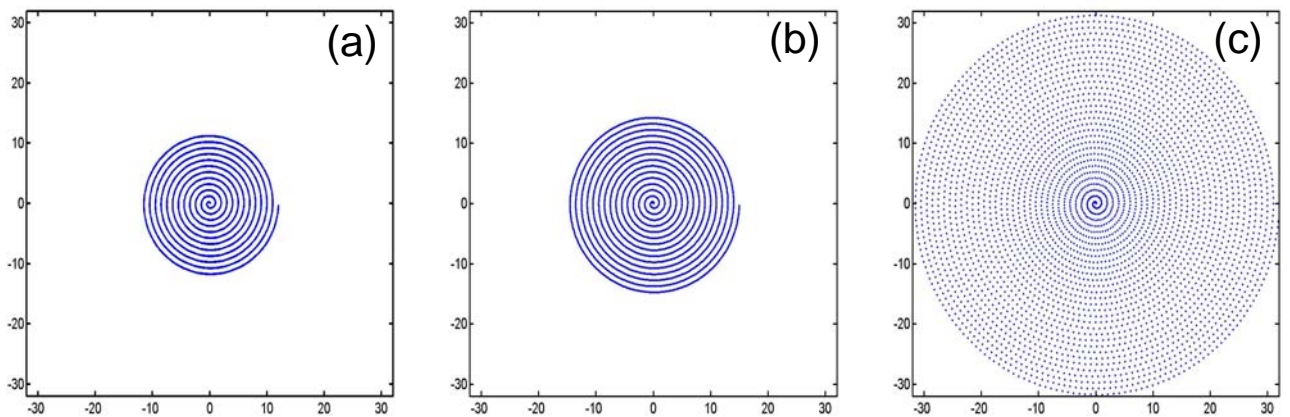


Fig. 4

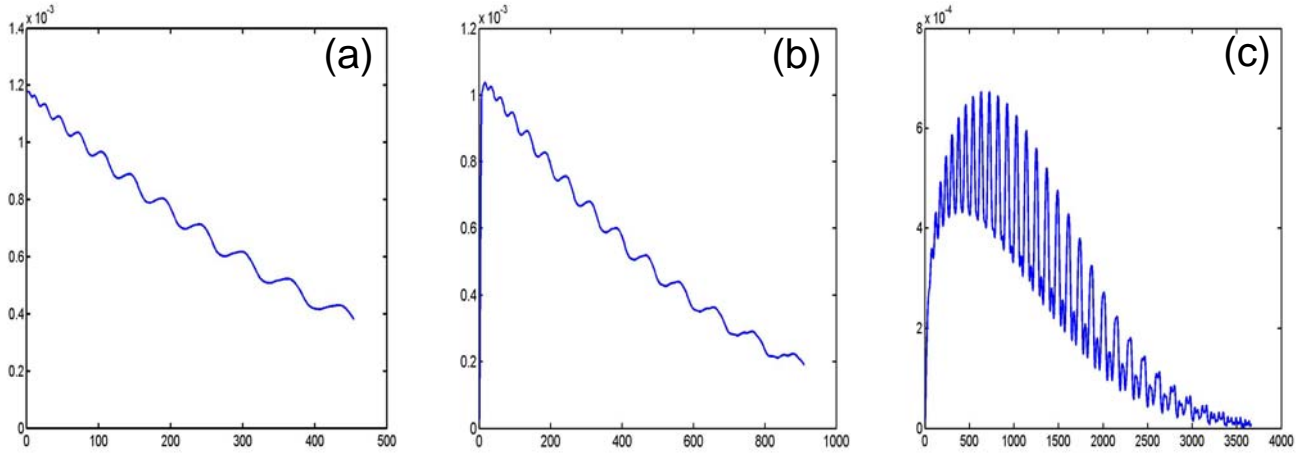


Fig. 5

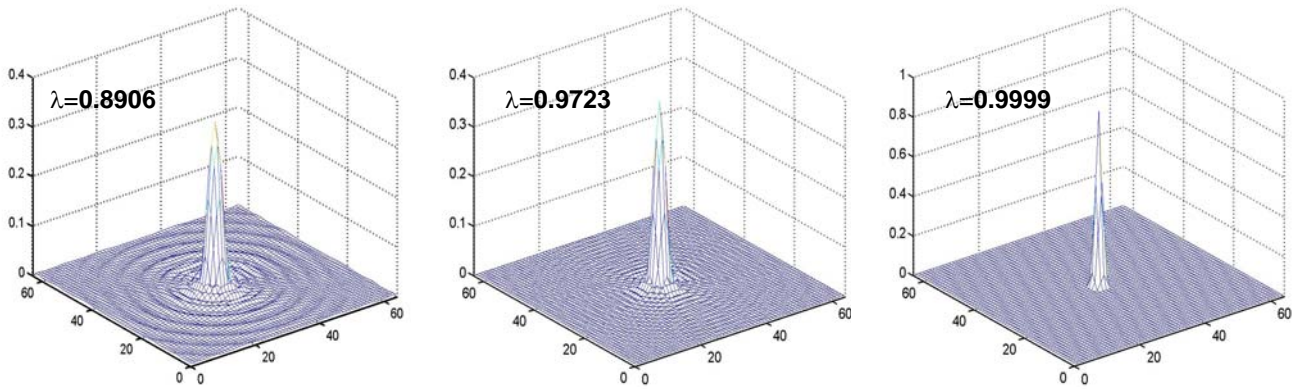


Fig. 6

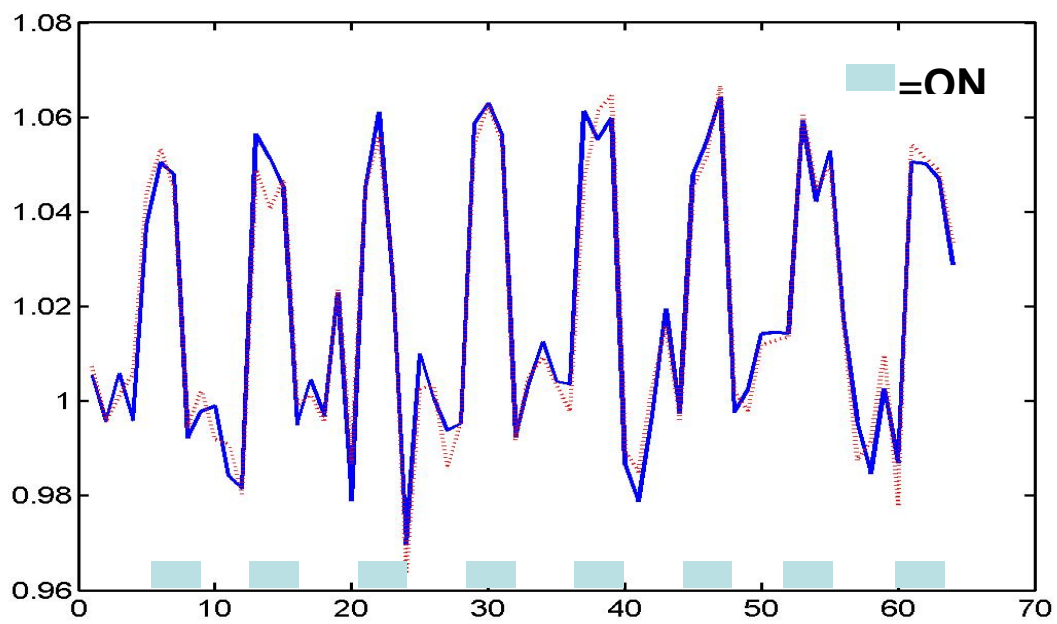


Fig. 7

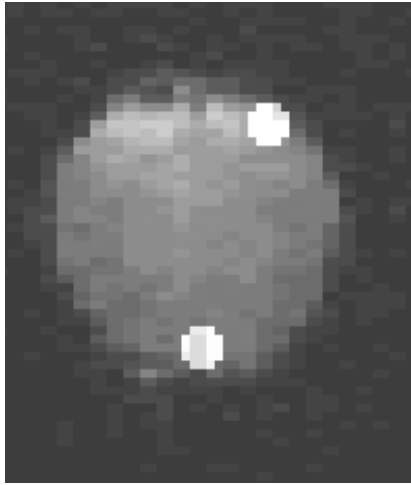


Fig. 8

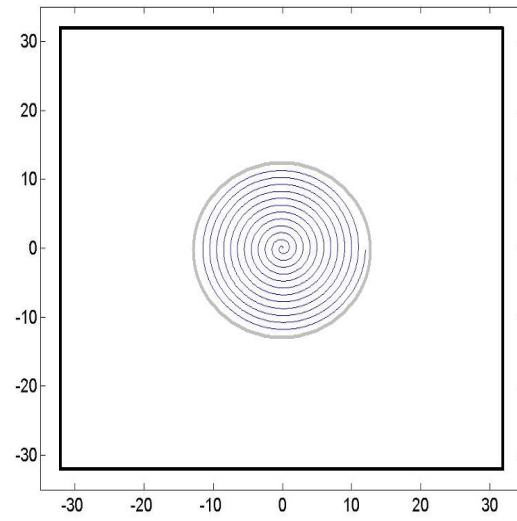


Fig. 9

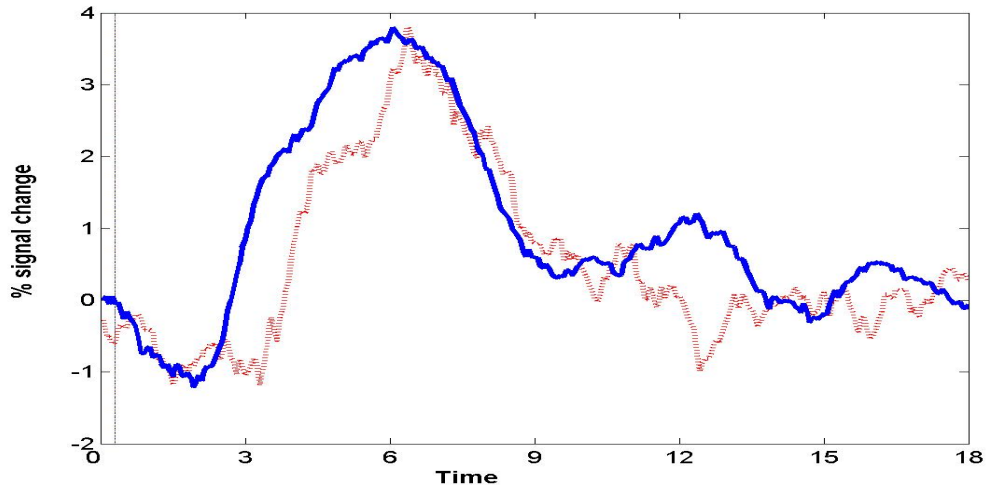


Fig. 10

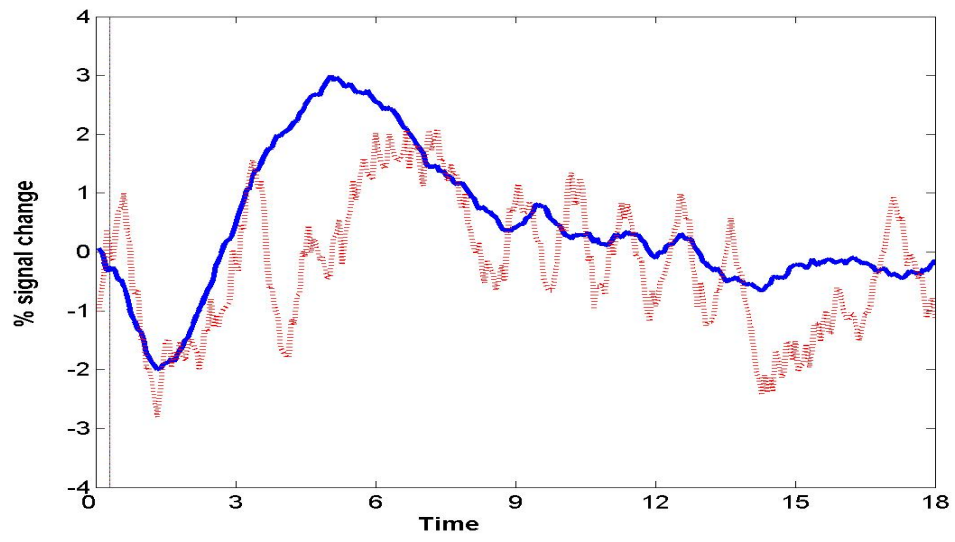


Fig. 11

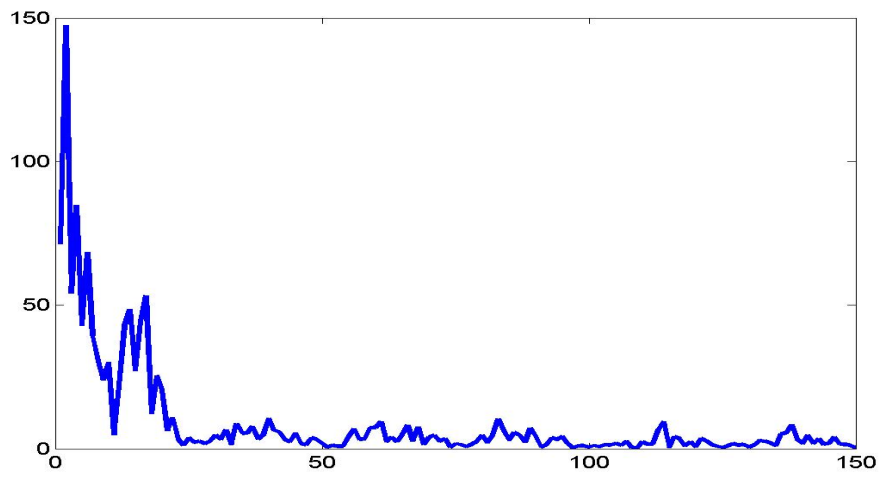


Fig. 12